JOURNAL OF GEOPHYSICAL RESEARCH, VOL. 102, NO. B4, PAGES 8121–8135, APRIL 10, 1997

Lateral variations in lowermost mantle shear wave anisotropy beneath the north Pacific and Alaska

Edward J. Garnero and Thorne Lay

Institute of Tectonics and Earth Sciences Department, University of California, Santa Cruz

Abstract. *S* waves recorded by long-period World-Wide Standardized Seismograph Network and broadband stations in North America for deep northwest Pacific subduction zone earthquakes provide evidence for anisotropy in the lowermost mantle shear velocity structure beneath the north Pacific and Alaska. Systematic delays of up to 4 s are observed between longitudinal components (*SV*) and transverse components (*SH*) of motion for core-reflected *ScS* waves as well as for core-grazing and diffracted *S* waves. The absence of significant splitting for *S* waves that have turning points more than a few hundred kilometers above the core-mantle boundary indicates that anisotropy is localized within the D″ region (the lowermost portion of the mantle). *SV*-*SH* differential arrival times for both *ScS* and S_{diff}, along with path length estimates assuming a 250 km thick D″ region, indicate spatial variations in the strength of shear wave anisotropy. The strongest anisotropy (1-1.5%) is found in the eastern part of the study area, with systematic reduction in magnitude toward the west. A transverse isotropy model can explain the data, with the velocity structure for horizontally polarized waves (V_{SH}) having a 2-3% discontinuous shear velocity increase at the top of D″ (as proposed in earlier studies of the region) and a similar structure for *S* wave particle motion in the direction normal to the core-mantle boundary (V_{SV}) but with the velocity jump at the top of D″ and the velocity within D″ being reduced from that for V_{SH} by 0.5-1.5 km/s. Large uncertainties exist for velocity gradients above and below the velocity jump, but the requirement of a reduced V_{SV} relative to V_{SH} in D″ is clear. Synthetic waveforms calculated by using separate isotropic structures for *SH* and *SV* match the observations well and constrain the basic anisotropic structure, because the shear waves all traverse the region with near-grazing geometries. The study area exhibits strong lateral variations in lower mantle shear velocity structure and variable thickness of the D″ layer. Topography of the D″ layer is not well resolved (because of trade-off with volumetric heterogeneity).

Introduction

Resolving the detailed seismic velocity structure at the base of the mantle is important, as this region is believed to play a major role in the mantle convection system. In the past decade a multitude of seismic investigations have resulted in a picture of diverse lowermost mantle properties (see review by *Loper and Lay* [1995]). The bottom several hundred kilometers of the mantle have long been known to be anomalous in relation to the overlying mantle, leading to the separate designation as the D″ region by *Bullen* [1949]. In addition to the anomalously low seismic velocity gradients that characterize D″, a rapid increase (2-3%) in velocity at the top of the D″ region has been detected in several different areas (see reviews by *Nataf and Houard* [1993] and *Lay* [1995]). This discontinuity has most commonly been observed in regions where large-scale tomographic models indicate that lower mantle velocities are higher than the global average. In contrast, regions with large-scale low velocities, such as beneath the central Pacific, have only intermittent or nonexistent discontinuities and a thin (5-40 km), laterally variable ultralow-velocity layer (10% *P* wave reductions) just above the core [*Garnero and Helmberger*, 1995, 1996; *Mori and Helmberger*, 1995].

The presence of lower mantle heterogeneity has been demonstrated at short (10-50 km) wavelengths [e.g., *Haddon and Cleary*, 1974; *Doornbos*, 1974; *Menke*, 1986a, b; *Bataille and Flatte*, 1988; *Weber*, 1993], at intermediate (100-1000 km) wavelengths [e.g., *Mitchell and Helmberger*, 1973; *Chowdhury and Frasier*, 1973; *Müller et al.*, 1977; *Lay*, 1983; *Lavely et al.*, 1986; *Schlittenhardt*, 1986; *Wysession and Okal*, 1988, 1989; *Weber and Kornig*, 1990, 1992; *Woodward and Masters*, 1991; *Revenaugh and Jordan*, 1991; *Wysession et al.*, 1992, 1994; *Garnero and Helmberger*, 1993; *Krüger et al.*, 1993, 1995], and at very long (>2000 km) wavelengths [e.g., *Dziewonski*, 1984; *Dziewonski and Woodhouse*, 1987; *Inoue et al.*, 1990; *Tanimoto*, 1990; *Masters and Bolton*, 1991; *Masters et al.*, 1992; *Su and Dziewonski*, 1991, 1992; *Rogers*, 1993; *Su et al.*, 1994; *Liu and Dziewonski*, 1994]. Lateral and radial variations in structural features of D″, coupled with the

Paper number 96JB03830.
0148-0227/97/96JB-03830$09.00

evidence for strong heterogeneity at many scale lengths, suggest a dynamically active D″ region.

Our understanding of the structural complexity of D″ has been expanded by recent observations of shear wave splitting (usually involving delay of onset of the *SV* component of motion as compared to the *SH* component) for core-grazing and diffracted waves [*Vinnik et al.*, 1989, 1995; *Lay and Young*, 1991; *Maupin*, 1994; *Matzel et al.*, 1996; *Kendall and Silver*, 1996]. Earlier work documented similar splitting for core-reflected *ScS* waves [*Mitchell and Helmberger*, 1973; *Lay and Helmberger*, 1983b]. The early studies of *ScS* waveform splitting explored models with complex isotropic structures, such as a very thin (20 km) high-velocity layer just above the core, which can produce an apparent delay of *SV* in relation to *SH* as a result of waveform interference phenomena. However, such models have not been able to account for the diffracted wave observations, so it appears likely that anisotropy (either mineralogical or structural) is present in some regions of D″. At this time there is great uncertainty in the cause of anisotropy in D″, primarily due to our limited knowledge of mineralogical properties, thermal and melting conditions, and dynamic processes in the region [e.g., *Wysession*, 1996; *Kendall and Silver*, 1996]. Making progress in this area will require both new seismological constraints on the anisotropic structure and mineral physics and dynamical constraints on properties of D″.

In this paper we combine two types of shear wave splitting information (differential travel times and waveforms) from core-reflected (*ScS*) phases and core-grazing (*S*) and diffracted (S_{diff}) phases (Figure 1) to investigate D″ anisotropy. We concentrate on the region beneath the north Pacific and Alaska, primarily because of the good ray path coverage for this region. We obtain a map of lateral variations in anisotropy in our study area and discuss possible relationships to variations in D″ thickness and lowermost mantle volumetric heterogeneity. Finally, we examine a few examples of shear wave observations from other regions and consider the possible relationship of anisotropy to large-scale lower mantle heterogeneity.

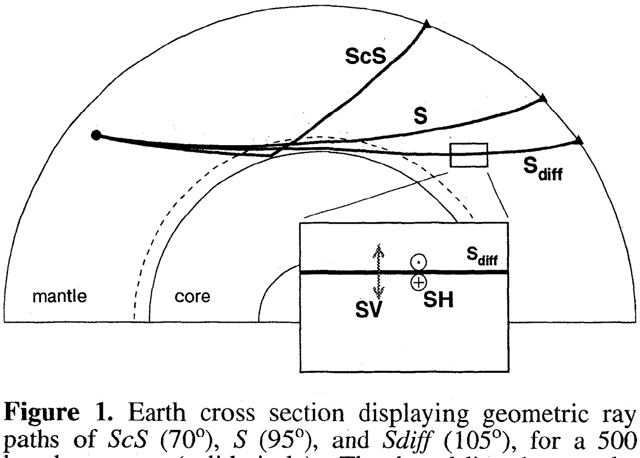

Figure 1. Earth cross section displaying geometric ray paths of *ScS* (70°), *S* (95°), and *Sdiff* (105°), for a 500 km deep event (solid circle). The dotted line denotes the top of the D″ layer. The inset illustrates the geometry of *SV* (longitudinal) and *SH* (transverse) particle motion.

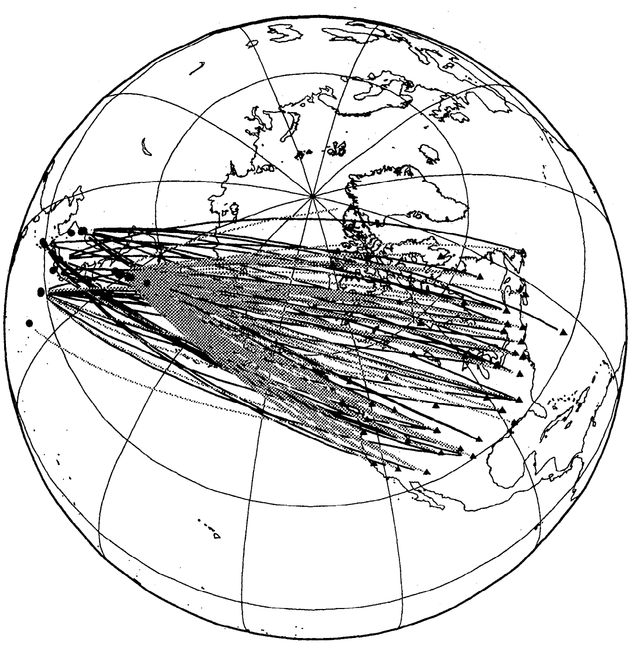

Figure 2. Great circle projections of *ScS* (shaded lines) and S_{diff} (solid black lines) wave paths between events (circles) and receivers (triangles).

Data: *S* Wave Splitting Observations

ScS and S_{diff} phases from deep focus events in the northwest Pacific subduction zones recorded at North American stations have raypaths that traverse the D″ region beneath the north Pacific and Alaska (Figure 2). The ray coverage in this region is relatively dense, although there is very limited azimuthal sampling. Our primary objective is to document spatial trends in shear wave splitting due to D″ anisotropy. Given the lack of crossing ray coverage, our resolution of structural features is limited to long wavelengths (>1000 km), and we cannot hope to fully characterize general anisotropic parameters (such as azimuthal anisotropy). We used data from 23 events (Table 1) recorded at 46 World-Wide Standard Seismograph Network (WWSSN) and broadband stations. The long-period (LP) WWSSN data have previously been studied by *Lay and Helmberger* [1983a, b], *Young and Lay* [1991], and *Lay and Young* [1991]. Our data selection was guided by the following requirements: well-recorded *SH* and *SV* arrivals (as defined in the great circle reference frame), good signal-to-noise ratio, and simple waveforms indicative of simple source rupture process. Nine of the events in Table 1 provided *ScS* observations and 12 events provided S_{diff} data.

Examples of *ScS* waveforms with shifts between the peak arrivals of ScS^{sv} and ScS^{sh} are presented in Figure 3. The map shows the corresponding paths. The shift between *ScS* arrivals on the separate components is measured by picking the peaks of the signals, as the onsets are difficult to measure. The accuracy in picking the peaks is within ±0.5 s for most of the data, limited mainly by the digitization noise and de-skewing required for WWSSN data. Examples with small, large, and intermediate degrees of *ScS* splitting are shown in Figure 3.

Table 1. Event Information

Date	Latitude, deg	Longitude, deg	Depth, km	Data[a]	ScS[b]	S[c]	SV[d]
Sept. 21, 1965	28.96	128.23	195	ww	0	3	0
Aug. 13, 1967	35.43	135.49	367	ww	0	4	1
May 14, 1968	29.93	129.39	162	ww	0	6	0
Aug. 15, 1969	21.57	143.10	320	ww	1	0	0
Sept. 5, 1970	52.28	151.49	560	ww	26	0	0
Jan. 29, 1971	51.69	150.97	515	ww	12	0	0
May 27, 1972	54.97	156.33	397	ww	10	0	0
Aug. 21, 1972	49.47	147.08	573	ww	18	1	0
Jan. 31, 1973	28.22	139.30	508	ww	0	4	3
July 28, 1973	50.45	148.92	585	ww	16	0	0
Sept. 10, 1973	42.48	131.05	552	ww	0	7	2
Feb. 22, 1974	33.17	136.98	391	ww	1	5	0
June 29, 1975	38.79	130.09	549	ww	0	1	0
Dec. 12, 1976	28.04	139.67	503	ww	3	1	0
March 9, 1977	41.66	131.05	556	ww	0	2	0
May 13, 1977	28.42	139.59	448	ww	2	8	7
April 24, 1984	50.12	148.75	582	ww	0	1	2
Oct. 30, 1992	29.97	138.93	406	bb	0	6	0
Jan. 18, 1993	18.38	145.71	169	bb	0	5	0
Jan. 19, 1993	38.70	133.50	460	bb	0	6	0
Oct. 11, 1993	32.30	137.90	350	bb	0	7	0
March 31, 1994	-21.70	-179.70	600	bb	0	14	0
May 10, 1994	-28.50	-63.06	605	bb	0	12	0

[a] ww, WWSSN LP data; bb broadband data.
[b] Number of records analyzed for ScS^{sv}-ScS^{sh} splits (for D″ anisotropy).
[c] Number of records analyzed for S_{diff}^{sv}-S_{diff}^{sh} splits (for D″ anisotropy).
[d] Number of records with diagnostic S_{diff}^{sv} waveforms (for D″ discontinuity structure).

At the two larger distances, *SKS* is present in the longitudinal component signal, and waveform modeling of the wave train aids in proper phase identification and accounting for interference effects [e.g., *Lay and Helmberger*, 1983b; *Lay and Young*, 1986]. Data for which it is difficult to rule out *SKS* interference with ScS^{sv} are omitted from our analysis. Small offsets in the ScS^{sh} and ScS^{sv} peaks can occur because of a phase shift between the *SV* and *SH* components at large incidence angles. When coupled with *SKS* interference of ScS^{sv}, this offset for the isotropic structure SYLO [*Young and Lay*, 1990] is non-zero between 65° and 85°, reaching a maximum of -0.4 s near 70° (ScS^{sv} arriving before ScS^{sh}). All of our ScS^{sv}–ScS^{sh} times have been corrected for this effect, with SYLO used for the corrections. Note that there is no shift of the peaks of direct *S* in these data, which indicates an isolated effect on the *ScS* arrivals.

Splitting effects from typical upper mantle anisotropy are usually of the order of only 1 s [e.g., *Silver*, 1996] and should produce little effect on WWSSN long-period recordings. A routine diagnostic for detecting upper mantle anisotropy is the presence of *SKS* energy on the transverse (*SH*) component of motion, since *SKS* should be longitudinally (*SV*) polarized in an isotropic medium. For the epicentral distance range of our core-grazing and diffracted *S* waves (90°–105°), *SKS* is readily observed but usually has little or no energy on the long-period WWSSN *SH* component [e.g., *Lay and Young*, 1991]. This behavior, however, does not preclude the presence of upper mantle anisotropy (and its effects on the data), since the source-receiver wave path geometry may be aligned with the orientation of fast or slow axes of anisotropy (which would simply differentially shift the components of motion). Our *ScS* data, on the other hand, from distances of 45°–80°, are always preceded by clear *S* arrivals, and we can compare the *S* and *ScS* waveforms to see whether there are differences in behavior. When we observe strong shifts in the arrival times of *SV* components of *ScS* (ScS^{sv}) in relation to *SH* components (ScS^{sh}), we assess whether there is any comparable shift of components of direct *S*, usually finding none. Thus the shear wave splitting must occur where the *S* and *ScS* paths are quite different, indicating a lower mantle origin.

These empirical approaches are not perfect controls on receiver anisotropy (splitting depends on incident polarization angle), but the fact that the observations of interest involve *ScS* split times as large as 4 s (with no associated *S* wave splits) suggests that receiver effects are at most minor perturbations on the observations. Nonetheless, the sites of several stations used in this study have been analyzed for upper mantle anisotropy in previous studies (for a review, see *Silver* [1996]). In fact, 40% of our data is at stations where corrections are possible. While we cannot yet correct the other 60% of

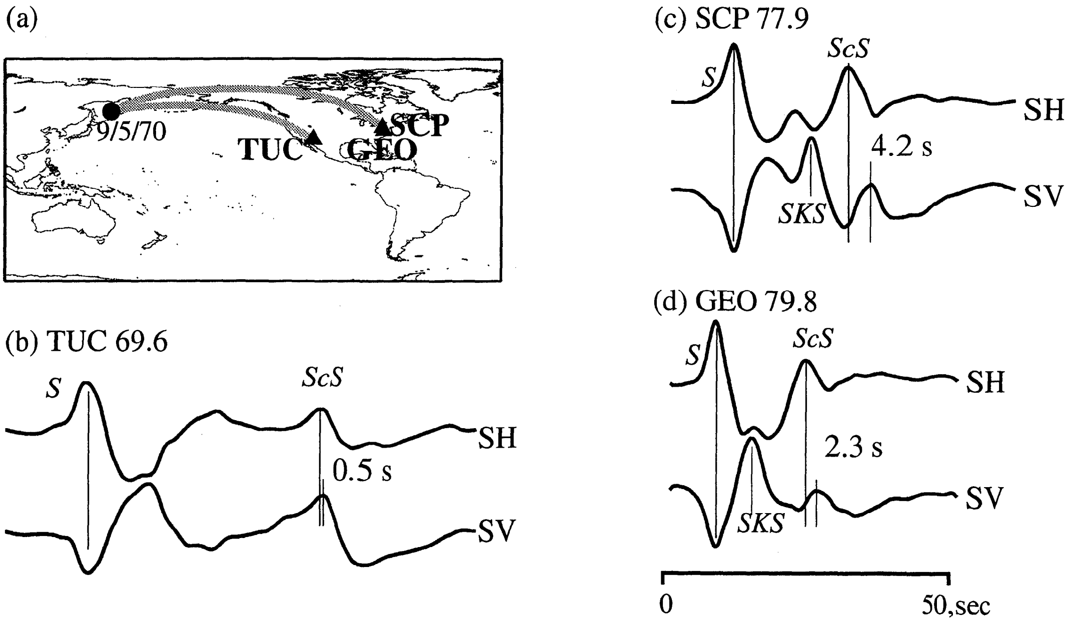

Figure 3. (a) Map showing wave path geometry between event 9/5/70 (circle) and three receivers (triangles). (b, c, d) *SH* and *SV* long period WWSSN recordings of *S* and *ScS* for station TUC at 69.6°, station SCP at 77.9°, and station GEO at 79.8°, respectively. Amplitudes are normalized to unity. ScS^{sv}-ScS^{sh} splits are indicated in the figure.

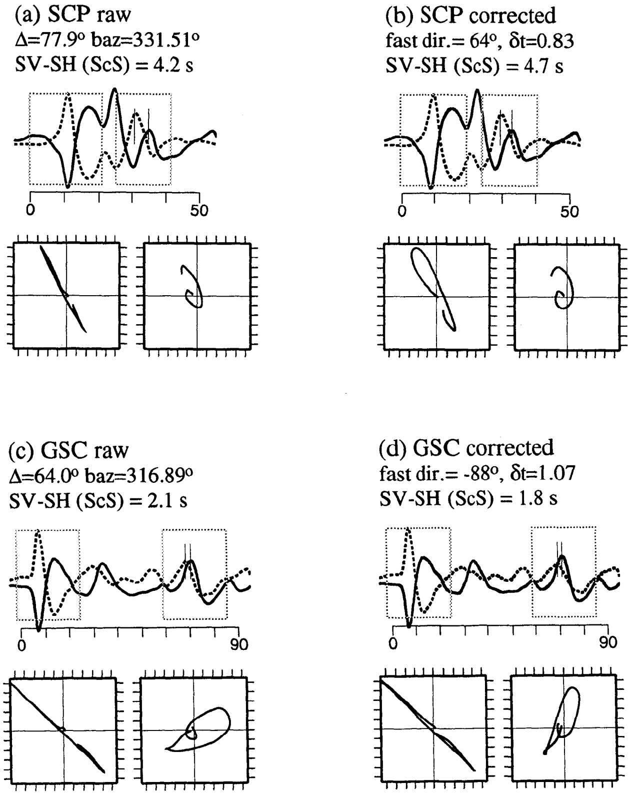

Figure 4. (a) Raw *SV* (solid) and *SH* (dashed) traces, showing *S* (first box) and *ScS* (second box) for observation SCP, event 9/5/70. Amplitudes are normalized to unity in plot. Particle motions for boxed time window are show below the traces, *S* first, *ScS* second. (b) Records from Figure 4a corrected for upper mantle anisotropy and particle motions. (c, d) Same as above except for record GSC, event 9/5/70. See text for details.

our data, it is still important to assess the effectiveness of applying the corrections where possible.

Figure 4 displays two examples from our *ScS* data set, as well as some of the issues that arise in correcting for upper mantle anisotropy. Figure 4a shows a raw record at station SCP (event 9/5/70, same record as in Figure 3c). The *S* and *ScS* arrivals are separately boxed and display coincident *S* peaks (first arrival) and *ScS* peaks separated by over 4 s. *ScS* is delayed on the *SV* component (solid) in relation to that on *SH*. The particle motions for the time window in each box are shown below the traces: *S* waves display linear motion, and *ScS* displays elliptical motion (with some *SKS* contamination to *ScS*). When corrected for anisotropy at SCP, i.e., back rotated to the fast polarization direction (64°), and appropriately time shifted (by 0.83 s), then rotated back to the back azimuth, the *ScS* split increases by 0.5-4.7 s (as measured by [ScS_{SV}-S_{SV}]-[ScS_{SH}-S_{SH}]). Also, the *S* wave particle motion now becomes elliptical, impling anisotropy somewhere other than D″ or the upper mantle. *ScS* particle motion appears slightly more elliptical, but interpretation of such is precarious because of possible *SKS* contamination. This record is an example in which the correction for upper mantle anisotropy may not be appropriate for the LP WWSSN data. Figures 4c and 4d present an example in which the correction does not significantly perturb the *S* wave particle motion from linearity and only slightly reduces the ellipticity of *ScS* particle motion. Also, as the text in the figure indicates, the fast polarization angle of −88° and δt=1.07 s applied to the record (at back azimuth 316.89°) results in a reduction of the magnitude of the *ScS* split from 2.1 to 1.8 s. The 0.3 s reduction in split is actually below our picking uncertainty of ±0.5 s, but nonetheless represents an example in which the correction may be appropriate.

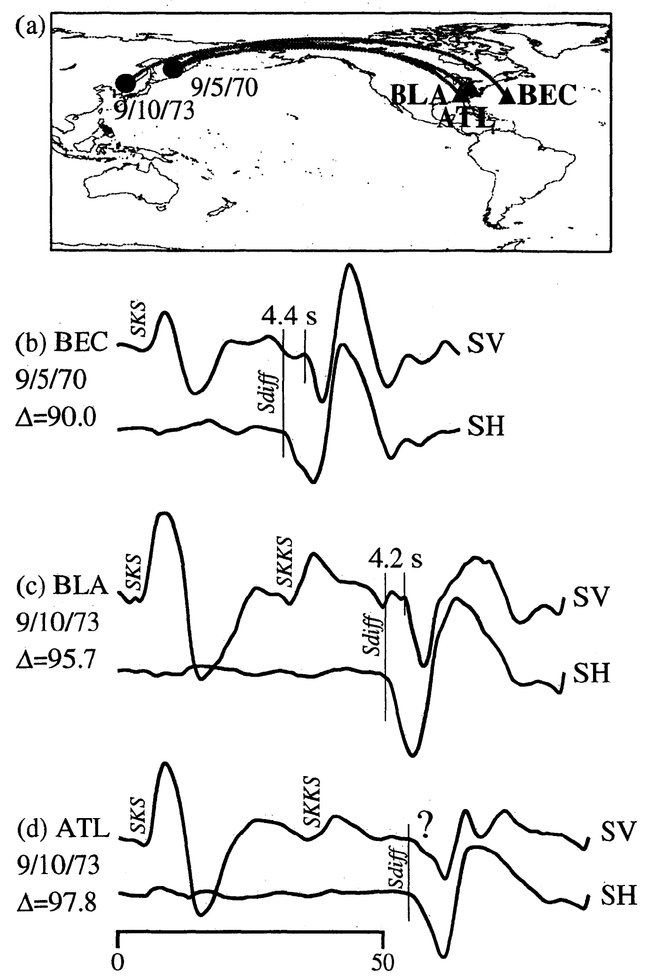

Figure 5. (a) Map showing wave path geometry between two events (circles) and three receivers (triangles). (b, c, d) *SH* and *SV* long period WWSSN recordings of *SKS* and S_{diff} for event 9/5/70, station BEC, 90.0°; event 9/10/73, station BLA, 95.7°; and event 9/10/73, station ATL, 97.8°, respectively. Amplitudes are normalized to unity. S_{diff}^{sv}-S_{diff}^{sh} splits are indicated in the figure.

However, since (1) only a fraction of our data are correctable, (2) the corrected data display varied levels of appropriateness of such corrections (as indicated by creating elliptical *S* particle motions), (3) the corrections typically amount to less than ±0.5 s adjustments to the *SV-SH* travel time splits, and (4) at longer wavelengths (e.g., LP WWSSN), such upper mantle anisotropy contamination should be minimized [e.g., *Kendall and Nangini*, 1996], we do not attempt to apply corrections to our data here for shallow structure. Such corrections are necessary if the analysis is extended to broadband data; see for example, *Kendall and Silver* [1996], who studied Canadian recordings of South American events. Thus it is a fundamental assumption in this study that upper mantle anisotropy [e.g., *Silver and Chan*, 1988] does not play a dominant role in contributing to the splitting of the core-reflected and diffracted data seen on the long-period WWSSN data.

We use the notation "S_{diff}" to denote either core-grazing or core-diffracted data. In many cases the primary energy of the associated phase turns somewhat above the core-mantle boundary (CMB), and the signals are not actually diffracted. Our notation is simply intended to make it clear that we are referring to *S* waves that have bottoming depths in the D″ layer. Figure 5 displays examples of *SV* and *SH* components of S_{diff} waves, S_{diff}^{sv} and S_{diff}^{sh}, respectively. Figures 5b and 5c show clear delays of the onsets of S_{diff}^{sv} in relation to S_{diff}^{sh}. Figure 5d, however, shows a record with a complicated S_{diff}^{sv} waveform, which precludes confident estimation of differential behavior between S_{diff}^{sv} and S_{diff}^{sh}. As we stated above, *SKS* has insignificant energy on the tangential components of motion, indicating that upper mantle anisotropy is not important for these long-period observations.

Broadband data for our study area have been collected for recent events. Usually, only one or two deep earthquakes with suitable characteristics occur in a given year, so we do not have an extensive broadband data set. We use it here primarily for purposes of comparison with the

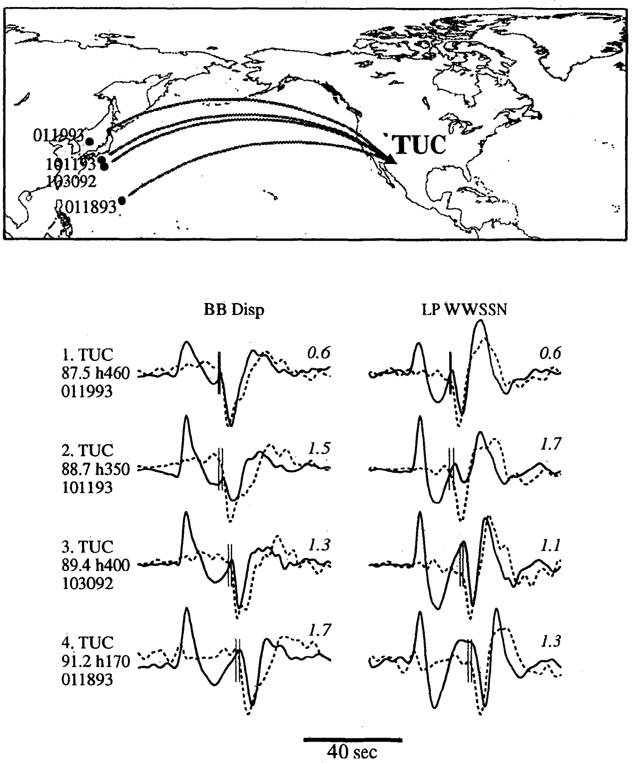

Figure 6. (Top) Great circle projections of broadband S_{diff} wave paths between events (circles) and station TUC (triangle). These paths correspond to data displayed in bottom half of figure: *SV* (solid lines) and *SH* (dashed lines) broadband recordings of *SKS* (first arrival on *SV* components) and S_{diff} (second dominant arrival on both components). Maximum amplitudes are normalized to unity. The four *SV-SH* pairs are displayed as raw broadband displacement (column 1), along with the same recordings filtered through a long-period WWSSN instrument response (column 2). The onsets of S_{diff}^{sv} and S_{diff}^{sh} are marked by short vertical lines, and the difference time between them is indicated by the number above the right of each record pair. Event dates, depths, and station names and epicentral distances are indicated to the left of the broadband records.

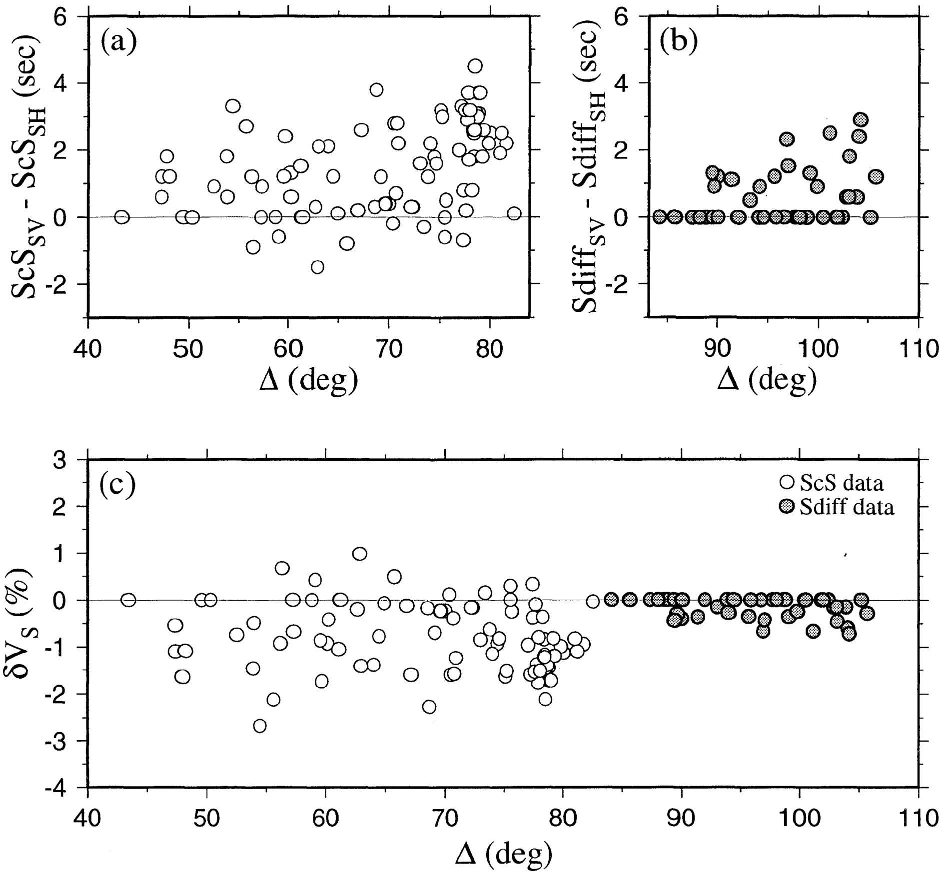

Figure 7. (a, b) Summary of all ScS^{sv}-ScS^{sh} and S_{diff}^{sv}-S_{diff}^{sh} splits, respectively, for the Alaska region. (c) Estimation of percent difference between the horizontal V_{SH} and vertical V_{SV} seismic velocities in the D″ layer, predominantly sampled by *SH* and *SV* motions, respectively.

older WWSSN observations. Figure 6 shows the path coverage and *SV* (solid) and *SH* (dotted) components of broadband displacements of S_{diff} and *SKS*. Station TUC has a predicted null offset of *SH* and *SV* due to upper mantle anisotropy [see *Silver*, 1996; *Barruol et al.*, 1997]. The onsets of S_{diff} on the two components of motion are indicated by vertical lines. These data are also shown after filtering by a long-period WWSSN instrument response. The *SV-SH* splitting measurements for the broadband and long-period WWSSN passbands agree well, indicating compatibility in the two data sets in addressing deep mantle anisotropy. The fourth record in Figure 6 has a somewhat shallow event depth (170 km) and displays some *SKS* contamination of the *SH* component, as well as a 0.4 s discrepancy in the measurement of the split on the two different band passes. This may be caused by anisotropy below the source in the subduction zone [e.g., *Russo and Silver*, 1994; *Fouch and Fischer*, 1996].

While the WWSSN data have a limited passband, they provide the advantage of a larger time span of signals recorded by a large number of seismographic stations. The magnitude of the splitting allows the WWSSN data to be used fruitfully, which is not the case for studying lithospheric splitting. On the other hand, detailed particle motion analyses of the digitized analog data cannot be done with confidence, because of possible absolute amplitude errors in the original paper records. Such analyses can only be applied to the more limited quantity of broadband data.

Having made many measurements of *SV-SH* differential arrival times for the core-reflected and diffracted data, we seek any systematic trend with distance that would suggest a one-dimensional structure. The splitting measurements are summarized in Figure 7. Figure 7a shows ScS^{sv}-ScS^{sh} times. Most differential times are positive, averaging about 1.3 s. Very few of the observations indicate ScS^{sv} arrivals earlier than ScS^{sh} (negative differential times), and most of these are close to the noise level. Figure 7b summarizes S_{diff}^{sv}-S_{diff}^{sh} times. More than half the data show no delay in S_{diff}^{sv} relative to S_{diff}^{sh}. Figures 7a and 7b separately suggest modest increases in splitting with distance, although there is substantial scatter and a significant number of observations at each distance with no splitting. A systematic increase in splitting with distance would be expected if there is a uniform layer of anisotropy. However, both the scatter and the lack of a significant increase in splitting for S_{diff} arrivals in relation to *ScS*, despite the longer path lengths of the former in D″, make it clear that any one-dimensional model will be unable to account for the data.

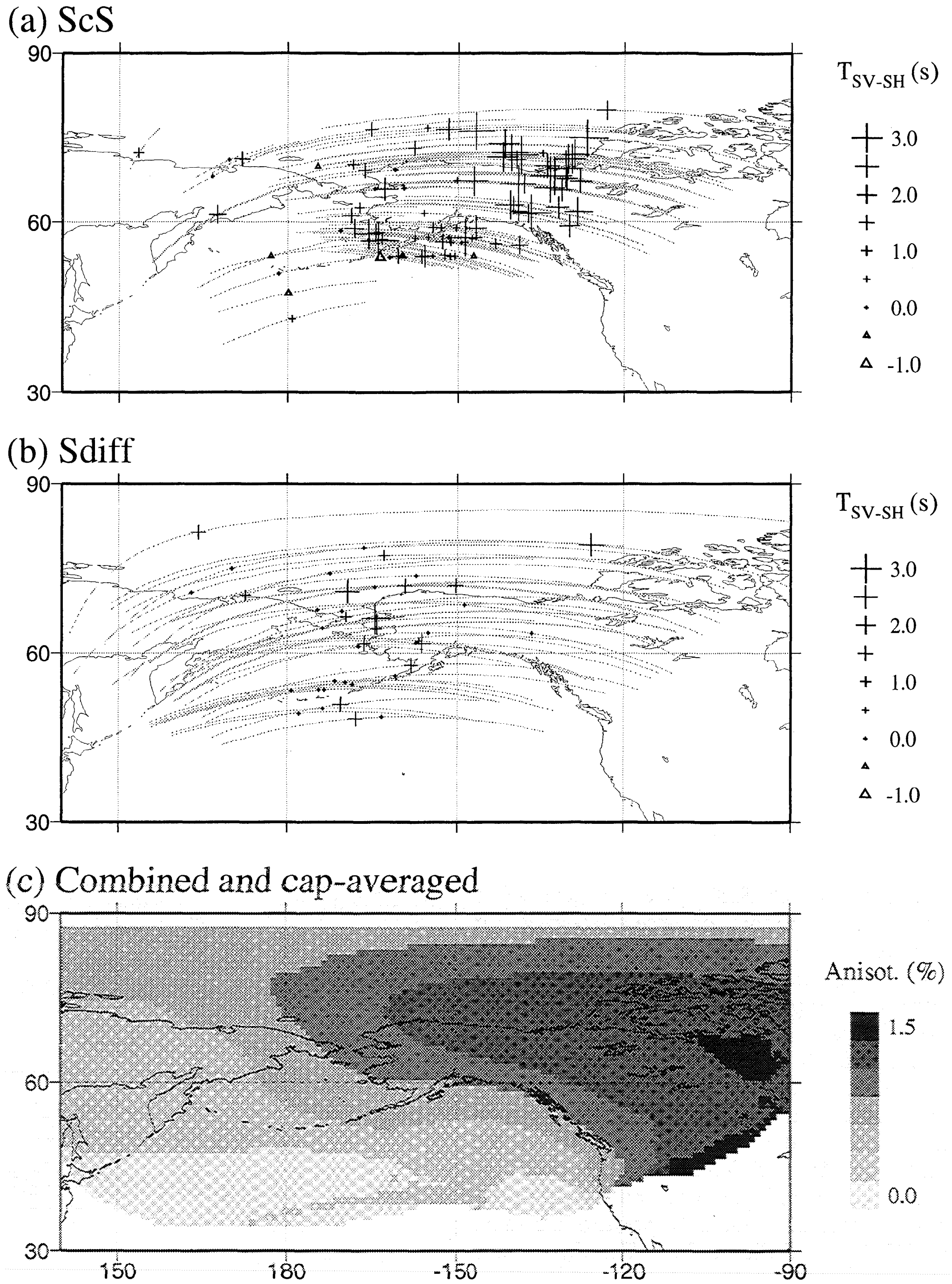

Figure 8. (a) Delays of ScS^{sv} relative to ScS^{sh} (crosses and triangles, scaled to magnitude of delay) plotted at CMB *ScS* reflection locations (data from Figure 7a). Also shown are the *ScS* paths in D″. (b) Same as Figure 8a except for S_{diff} (data from Figure 7b). (c) Gaussian cap average of anisotropy estimates of data in Figures 8a and 8b. Cap radius is 10°.

To quantify this finding, we computed D″ path lengths for the data in Figures 7a and 7b, using geometric ray paths through a previously proposed one-dimensional lower mantle shear velocity model for this region (model SYLO of *Young and Lay* [1990]). This model has a 2.75% velocity increase 243 km above the CMB and is similar to model SLHO, which was previously proposed by *Lay and Helmberger* [1983a]. The D″ path length estimates, combined with the travel time differentials of Figures 7a and 7b, have been converted to relative velocity perturbations, δV_s, using SYLO as a reference structure. The values of δV_s represent the average velocity reduction/increase experienced by *SV* particle motion in relation to that of *SH* along the entire D″ portion of *ScS* or S_{diff} wave paths. These velocity perturbations are plotted in Figure 7c, giving a measure of anisotropy as a function of epicentral distance for our data. The increases with distance suggested in Figures 7a and 7b are suppressed by normalizing the data by D″ path length, and it is clear that the *ScS* data sample a region with stronger anisotropy than the the core-grazing data.

Several inherent assumptions underly the conversion to velocity perturbations in Figure 7c. The cause of the observed shear wave splitting is constrained to the D″ layer, which directly influences the magnitude of the velocity perturbations. This assumption is supported by the fact that the core-grazing waves are the closest direct *S* waves to exhibit splitting. However, it is not obvious that the D″ layer has uniform thickness that the anisotropy is uniformly distributed within the layer. We also assume that, to first order, the polarized motion of ScS^{sv} and S_{diff}^{sv} only senses the velocity for particle motions in the direction normal to the CMB, V_{SV}. A significant portion of the D″ path of S_{diff} is nearly parallel to the CMB, as is the case for larger distance *ScS* waves; thus associated *SV* particle motion is close to normal to the CMB. Nonetheless, some underestimation of the magnitude of V_{SV} may exist because of this approximation, though this is very likely a minor affect [e.g., *Doornbos et al.*, 1986]. Thus the values in Figure 7c may represent a lower bound of the difference between V_{SV} and V_{SH} within D″. We basically are interpreting the travel time differentials as the result of the special case of anisotropy called transverse isotropy, with $V_{SV} < V_{SH}$ [e.g., *Cormier*, 1986; *Doornbos et al.*, 1986]. In this case, treating the observations as naturally polarized with respect to the anisotropic structure appears warranted by the observations, but is difficult to fully validate this approach, given the limited bandwidth of the observations and the fact that arrival onsets are often difficult to pick with confidence (particularly for *ScS*). We do gain some confidence from the clean shift of onsets observed for many S_{diff} phases for the back-azimuth coordinate system. Detailed polarization analysis is required to explore for more general anisotropy [e.g., *Maupin*, 1994], but our data do not permit this.

It is clear that spatial variations in the magnitude of the transverse isotropy must be present. The *ScS SV-SH* travel times of Figure 7a are plotted at *ScS* CMB bounce points, along with *ScS* paths through D″, in Figure 8a. The figure displays ScS^{sv}-ScS^{sh} times that are small toward the west, large toward the east, and mixed in the center of the study region. Figure 8b presents the same for S_{diff} (*SV-SH* times of Figure 7b). The S_{diff} times also show some suggestion of this trend, though the S_{diff} midpoint coverage is more localized (coinciding with the region in which *ScS* splits are scattered), making quantification of such a trend difficult for Sd times alone. The *ScS* and S_{diff} velocity anisotropy estimates of Figure 7c were smoothed to obtain a map of the inferred long-wavelength trend of the data in the following manner: (1) assign anisotropy estimates for each path to locations at 1 degree increments along D″ wave paths; (2) Gaussian cap average the data, moving the cap over a 1 x 1 degree grid in the sampled area; and (3) apply the Gaussian cap averaging for a 10^o cap radius (Figure 8c). The map shows a systematic increase in anisotropy toward the east, with tapering to near zero on the western edge of the study area. The patterns reflect the fact that the *ScS* data with the strongest splitting are from the most northerly events in the Kurile subduction zone recorded by east coast stations, while more southerly events show both diminished *ScS* splitting at western stations and only modest splitting of S_{diff} at east coast stations.

In this section we have presented spatial variability of D″ anisotropy as implied by *SV-SH* splits of *ScS* and S_{diff}. The smoothing method employed yields an image with details that may of course differ from those of a formal inversion. An inversion of our data would not be meaningful, since we have very little crossing ray path coverage. Nonetheless, the long-wavelength trend displaying increasing anisotropy toward the east of our study area is robust. We will now incorporate this first-order finding into waveform predictions through models having reduced V_{SV} velocities relative to V_{SH} to pursue further details of the velocity structure.

Waveform Modeling of WWSSN Observations With *S* Wave Splitting

Records of S_{diff} data at distances less than 90^o show little evidence for shear wave splitting (e.g., see Figure 7b). Thus we have made the assumption that the anisotropy at the base of the mantle is in D″ (e.g., Figure 8). The exact nature of how V_{SV} departs from V_{SH} within the D″ layer has not been constrained in the approach of the previous section, and indeed there is little constraint provided by the travel time data. For waveform modeling we assume a constant reduction of V_{SV} relative to V_{SH} throughout D″. For example, Figure 9 displays model SYLO, our reference *SH* (V_{SH}) structure, along with three models: SYLO.75, SYLO.50, and SYLO.25, containing reductions in the magnitude of the SYLO velocity discontinuity and average velocity increase within D″ of 75%, 50%, and 25%, respectively. In the convention of Figure 8 these models correspond to anisotropy of -0.63% (SYLO.75), -1.25% (SYLO.50), and -1.88%

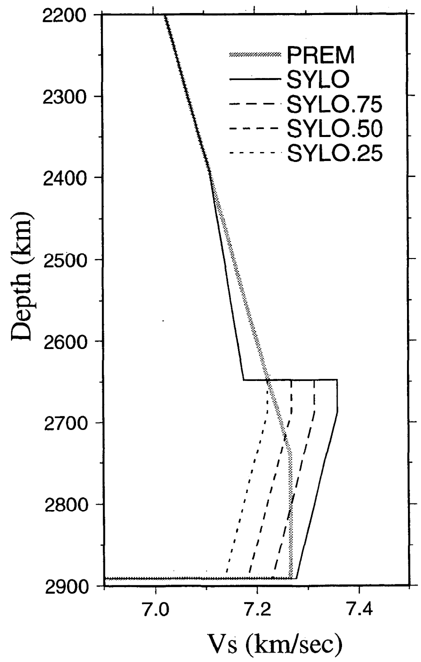

Figure 9. Velocity-depth profiles used in the reflectivity waveform modeling.

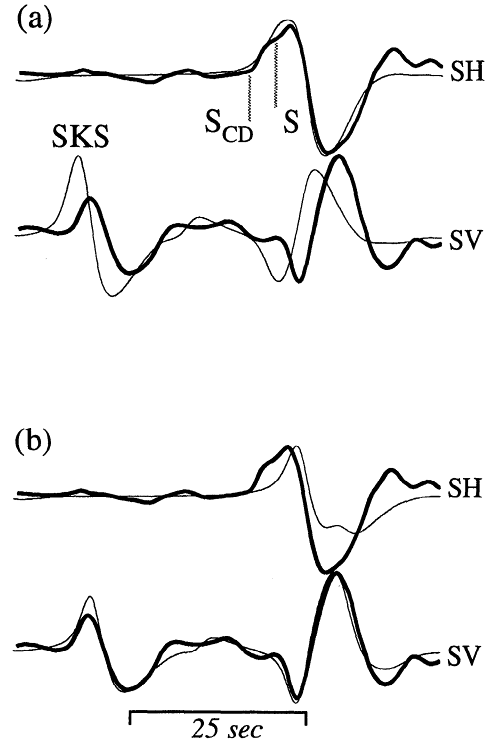

Figure 10. Comparison of observed (thick lines) and predicted (thin lines) *SH* and *SV* components of motion for station BEC at 90° with (a) model SYLO and (b) model SYLO.25. Maximum amplitudes are normalized to unity. See text for details.

(SYLO.25). Reflectivity synthetics [*Kind* and *Müller*, 1975; and *Müller*, 1985] are computed for these isotropic structures and used in the following manner: model SYLO is used to generate *SH* waveforms, and models SYLO.(75,50,25) are used to generate *SV* synthetics. This approach assumes that the *SV* particle motion velocity for the entire D″ path can be approximated by V_{SV}. As previously discussed, this assumption should be adequate for our purposes. Our modeling uses *P* wave velocities and densities from model PREM [*Dziewonski and Anderson*, 1981]. While fully anisotropic calculations can be made at much greater effort [*Matzel et al.*, 1996], the additional parameters involved even for transverse isotropy do not appear to be resolvable for data like ours, so we assume only one end-member transverse isotropy model by our modeling approach.

Figure 10 displays synthetic waveform comparisons with one of the S_{diff} observations of Figure 5b. Figure 10a compares observed *SH* and *SV* waveforms (thick lines) with predictions for model SYLO (thin lines). The S_{diff}^{sh} wave shape is well reproduced by SYLO, with the first arrival of the S_{diff}^{sh} pulse associated with energy (S_{cd}) traveling in the D″ fast layer, followed by energy refracted at the top of D″ (direct *S*). This constructive interference causes a distortion of the pulse, resulting in a weak, broadened upswing and a strong overshoot. This isotropic model predicts S_{diff}^{sh} arriving simultaneous to S_{diff}^{sv}, several seconds earlier than the observed S_{diff}^{sv}. Model SYLO.25 predictions, on the other hand, match the timing and shape of S_{diff}^{sv} (Figure 10b) but poorly match S_{diff}^{sh}. Thus, using two separate isotropic structures, i.e., SYLO for S_{diff}^{sh} and SYLO.25 for S_{diff}^{sv}, we can model the waveform example in Figure 10. In this fashion, all of the S_{diff} data in principle can be modeled by varying the magnitude of the reduction of V_{SV} in relation to V_{SH}. It is important to note that the identification of the specific triplication effects required to explain the *SH* waveform requires that the anisotropic structure coincide with the D″ discontinuity. The S_{cd} energy exists only because of the discontinuity, and it turns within a few tens of kilometers of this discontinuity in the SYLO model. Thus, for the corresponding *SV* energy to be delayed as observed requires that the discontinuity be weaker for *SV*. Can we simply eliminate the discontinuity for V_{SV}, as proposed in the study of *Matzel et al.* [1996]? As shown below, we cannot, for the *SV* data independently require the presence of a discontinuity at least in some regions. We chose to simply reduce the discontinuity to the extent needed to match the timing and wave shape but to allow the discontinuity to exist in both V_{SV} and V_{SH} structures.

A similar approach is taken to explain *ScS* data. Figure 11a displays the observed *SH* and *SV* waveforms for an observation at 80°. This observation has a 1.9 s delay of the peak of ScS^{sv} relative to ScS^{sh}. Figures 11b and 11c compare the observations with reflectivity synthetic seismograms for models SYLO, SYLO.50, and PREM. Model SYLO matches *ScS-S* separation on the *SH* component (Figure 11c) but therefore underpredicts the delay time of ScS^{sv} in relation to *S* (Figure 11b). SYLO.50 matches the ScS^{sv} waveform and timing but in turn

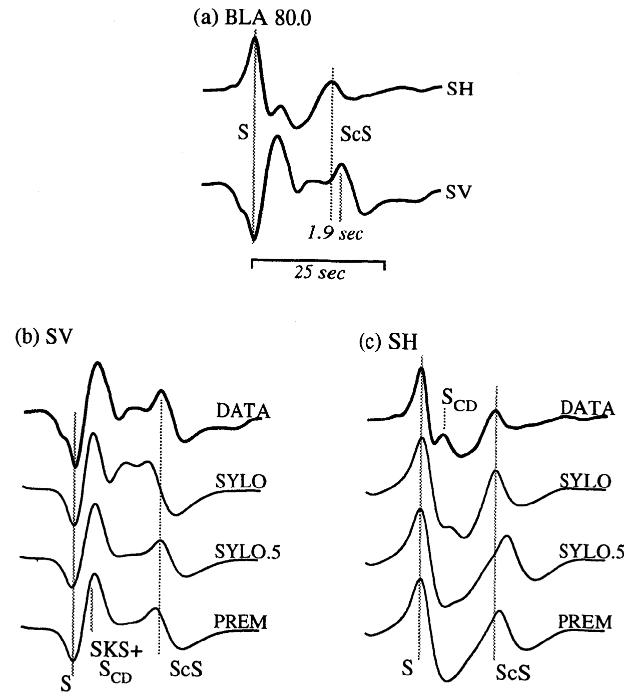

Figure 11. (a) ScS^{sh} and ScS^{sv} observations at station BLA. (b) Comparison of ScS^{sv} data (top, thick line) and reflectivity synthetics (thinner lines, three bottom traces) for models SYLO, SYLO.50, and PREM. (c) Same as Figure 11b except for ScS^{sh}. Maximum amplitudes are normalized to unity. See text for details.

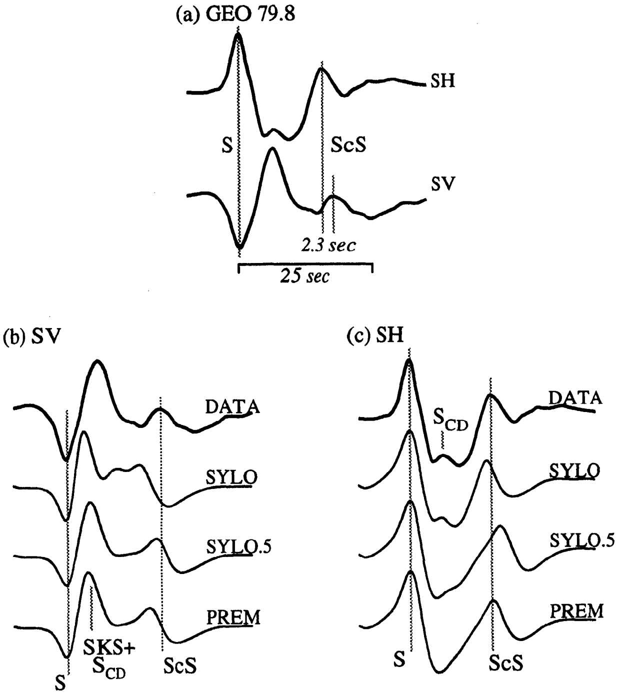

Figure 12. (a) ScS^{sh} and ScS^{sv} observations at station GEO. (b) Comparison of ScS^{sv} data (top, thick line) and reflectivity synthetics (thinner lines, three bottom traces) for models SYLO, SYLO.50, and PREM. (c) Same as Figure 12b except for ScS^{sh}. Maximum amplitudes are normalized to unity. See text for details.

predicts too late of an ScS^{sh} arrival. The D″ discontinuity structure in SYLO produces the S_{cd} arrival intermediate to S and ScS, which is in good agreement for the data and SYLO synthetics (Figure 11c). Note that the S_{cd} arrival is also present on the SV waveform (albeit complicated because of the presence of SKS in the same time interval), and model SYLO appears to predict too early of an S_{cd} arrival by about the same amount as ScS^{sv} is early. Weakening the discontinuity as in model SYLO.5 lines up both of these arrivals better but may weaken the S_{cd} arrival a bit too much in relation to the data. This result provides evidence that the discontinuity is present for both V_{SH} and V_{SV} structures. The isotropic reference model PREM does not produce splitting of the shear waves, nor does it predict the S_{cd} arrival. Anisotropic versions of a smooth model like PREM (or other models lacking a D″ discontinuity) can be found to fit the observed ScS^{sv} and ScS^{sh} waveforms, but these will necessarily not match the S_{cd} energy. As we will show in the next section, a V_{SV} discontinuity is necessary to explain many of the S^{sv}_{diff} observations.

Figure 12a shows another waveform with split ScS waveforms. The ScS^{sv}–ScS^{sh} differential time of 2.3 s can be fitted in with similar models as in Figure 11. Figure 12b shows the underprediction of the ScS^{sv}–S time (T^{sv}_{scs-s}) for model SYLO (and PREM). SYLO.50 more closely matches T^{sv}_{scs-s}, and the S_{cd} arrival is weak, as suggested by the data. SYLO does a good job at matching the observed T^{sh}_{scs-s} differential time (Figure 12c) as well as the overall SH wave shape, including the S_{cd} arrival. Note that both ScS^{sh} of SYLO and ScS^{sv} of SYLO.50 are predicted to arrive slightly earlier than the observed phases. This prediction illustrates a common feature of our data set: the various differential times between S^{sh}, S^{sh}_{cd}, and ScS^{sh} are on average fitted by SYLO, but small scale scatter about this reference model is ubiquitous [*Lay and Young*, 1996]. Nonetheless, the observed ScS^{sv}–ScS^{sh} time for the GEO record is well predicted by T^{sv}_{scs}(SYLO.50)–T^{sh}_{scs}(SYLO). For this region there is significant mid-mantle heterogeneity (generally with high velocity) [*Lay*, 1983; *Vidale and Lay*, 1993; *Grand*, 1994; *Liu and Dziewonski*, 1994; *Lay et al.*, 1997], which can perturb the direct S time, thus affecting ScS-S times. This should not affect our conclusions, since we are most concerned with the differential behavior between SH and SV components of motion.

Waveform Modeling of Diffracted S^{sv}_{diff}

Since our approach does not uniquely constrain the differential velocity structure between V_{SV} and V_{SH} within the D″ layer, it is instructive to consider additional waveform information. Previous studies of the V_{SH} structure in this region yielded models such as SYLO [*Lay and Helmberger*, 1983a; *Young and Lay*, 1990]. Subsequently, analysis of S^{sv}_{diff} for this region presented evidence for a similar, but deeper D″ discontinuity [*Lay and Young*, 1991] in some areas. We consider further

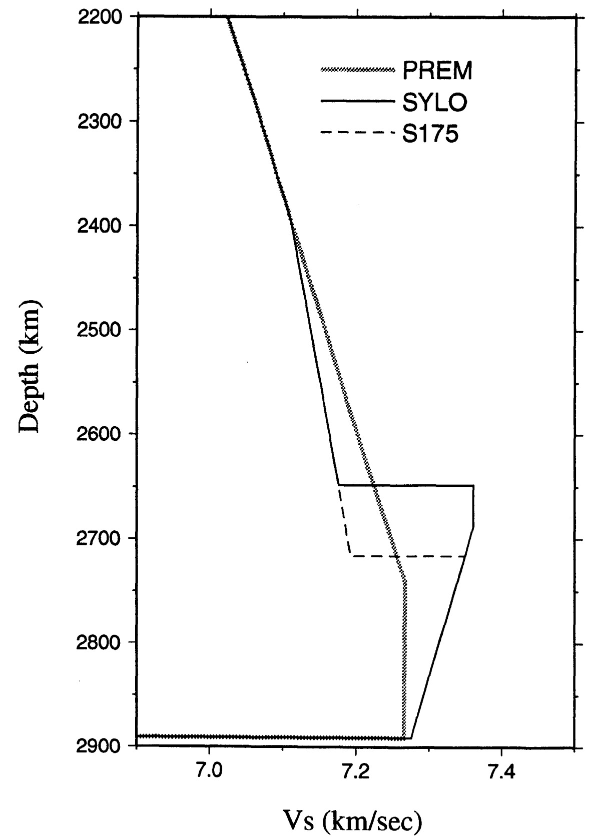

Figure 13. Velocity-depth profiles for models SYLO, S175, and PREM. The reduced thickness model S175 explains complicated waveform behavior in many of the observed S^{sv}_{diff} waveforms.

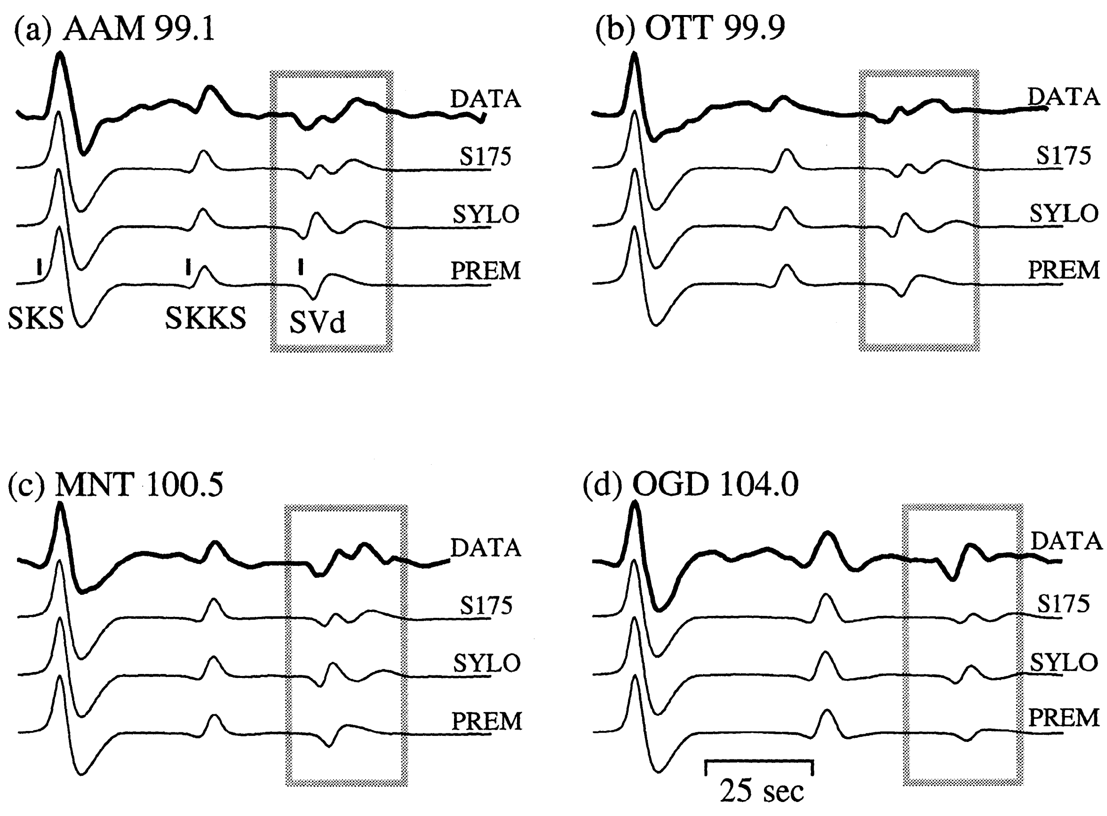

Figure 14. Observed (top thick trace) and reflectivity predicted (lower three traces) waveforms containing *SKS*, *SKKS*, and S_{diff}^{sv} (boxed). Records (a) AAM 99.1°, (b) OTT 99.9°, (c) MNT 100.5°, and (d) OGD 104° are all from event 5/13/77. Maximum amplitudes are normalized to unity.

these data, as they bear upon our parameterization of V_{SV} structure, and the issue of variability in the discontinuity in our study area.

A deeper D″ discontinuity model (S175) is compared with SYLO and PREM in Figure 13. The thickness of the D″ fast layer in S175 is 175 km, compared to 243 km in SYLO. *SV* component reflectivity predictions for these models are compared to S_{diff}^{sv} observations in Figure 14. At these distances (99°–104°), *SKS*, followed by *SKKS*, arrives before S_{diff}^{sv}, and the waveforms of these arrivals are insensitive to model differences in D″. However, larger-scale perturbations can significantly perturb *SKKS-SKS* times [*Garnero and Helmberger*, 1995]. S_{diff}^{sv}, on the other hand, is very sensitive to D″, and predictions for the various models differ significantly in wave shape (see highlighted regions in Figure 14). Observed S_{diff}^{sv} show a characteristic double trough, followed by a slightly longer period peak, in Figures 14a, 14b, and 14c. The general character of this wave shape is reproduced by model S175. Slight S_{diff}^{sv} time shifts are necessary to align observed and predicted S_{diff}^{sv} onsets. These correspond to *S-SKS* anomalies of 2-3 s, which are easily explained by the faster-than-average lower mantle and midmantle structure in this region. Thus time shifts to align the observed and predicted S_{diff}^{sv} onsets are permissible and do not affect the wave shape predictions. SYLO predictions over-predict the separation between the first and second pulses in S_{diff}^{sv} (which correspond to energy traveling in and above the D″ layer, respectively). An exception is the waveform of Figure 14d, in which S175 poorly matches the observation and SYLO produces a better fit. In all four cases the PREM wave shape is a simple pulse and poorly matches the observations (see also *Lay and Young*, [1991]). These observations demonstrate both existence of complexity in the V_{SV} structure, well accounted for by a class of discontinuity models similar to that found for V_{SH}, and the implication for the discontinuity depth to vary laterally in the study region. As was shown by *Lay and Young* [1991], the models that best fit the S_{diff}^{sv} waveforms do not always match the S_{diff}^{sh} waveforms very well, a suggestion that anisotropy is present even in the regions with thinner D″ layer.

Topography of D″

The D″ shear velocity structures of Figure 9 are used to explain the discrepant *SH* and *SV* times and wave shapes (e.g., Figures 10, 11, and 12), assuming the D″ thickness of SYLO (243 km). This thickness is necessary to reproduce observed S-S_{cd}-ScS times and waveforms on the *SH* component and is compatible with our path-averaging approach used to infer long-wavelength anisotropy patterns (of Figure 8c). However, that some of the S_{diff}^{sv} wave shapes necessitate a reduced thickness D″ layer (175 km, Figure 13) indicates the presence of lateral variations in D″ thickness, that is, D″ topography.

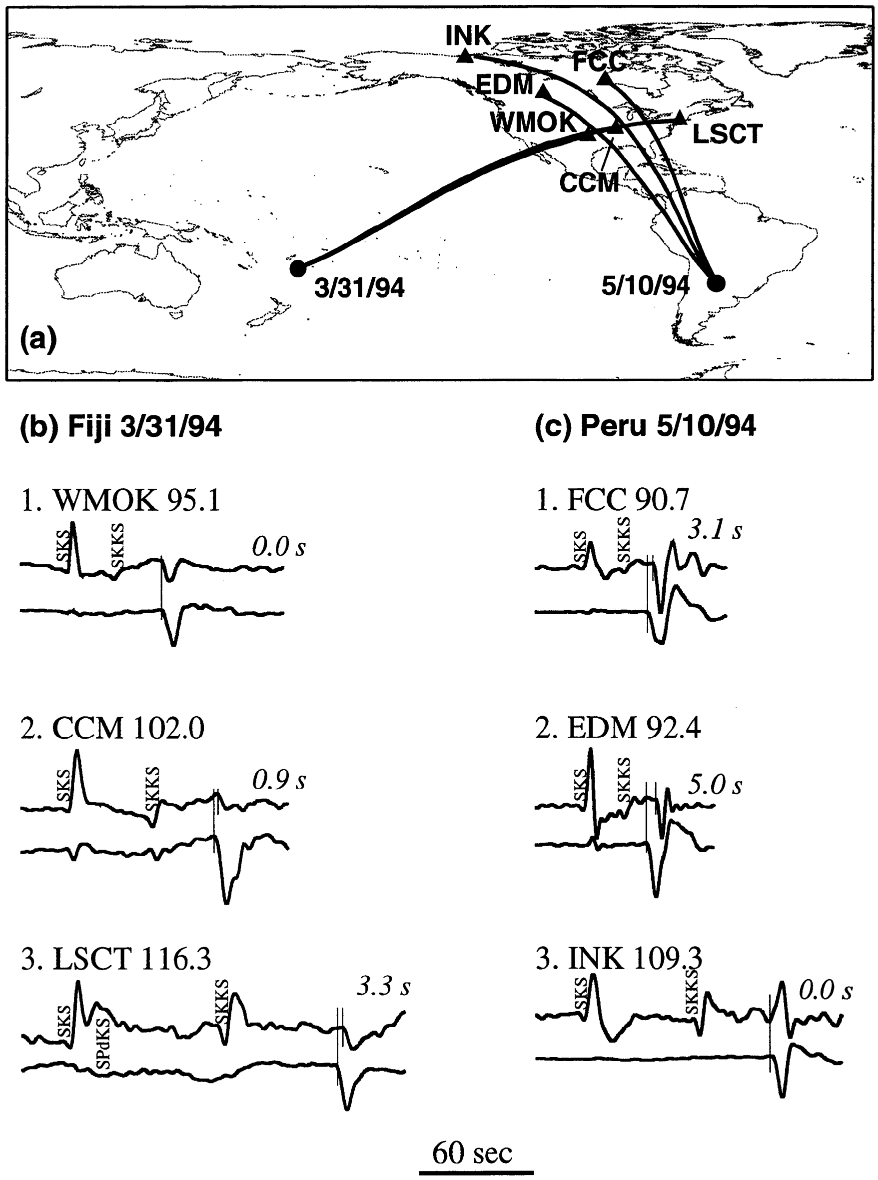

Figure 15. (a) Great circle projections of wave paths for which broadband S_{diff} waveforms are displayed below. (b) Three record pairs (*SV* is the top trace, and *SH* is the bottom trace of each pair) for the deep focus 3/31/94 Fiji event. (c) Three record pairs for the deep focus 5/10/94 Peru event. S^{sv}_{diff}-S^{sh}_{diff} splits are indicated by the number above the right corner of each record pair. The data have been corrected for upper mantle anisotropy.

There is mounting independent evidence suggesting topographic variations in the D″ discontinuity [e.g., *Weber*, 1993; *Kendall and Shearer*, 1994; *Kendall and Nangini*, 1996]. *Lay et al.* [1997] further pursue this issue for the same study area, using S_{cd}-*ScS* travel time residuals relative to SYLO. Using a total number of 158 high-quality measurements, they convert $\delta T_{scs-scd}$ residuals into D″ topography perturbations (relative to SYLO) in the same manner as *Kendall and Shearer* [1994]. For example, a relatively thin D″ layer will result in S_{cd} arriving closer in time to *ScS*, thus resulting in a smaller S_{cd}-*ScS* time, i.e., a negative $\delta T_{scs-scd}$ residual relative to a starting model such as SYLO. They find evidence for small-scale topography around the predominant thickness of 250-275 km, which is close to that of SYLO (243 km), with some suggestion of a thinner D″ layer (225-250 km) in the western part of the study area. However, direct trade-offs exist between volumetric and topographic heterogeneity in D″, and the issue is further complicated by the possibility of mid-mantle heterogeneity affecting direct *S* times [*Lay et al.*, 1997]. Because of such uncertainties we do not further pursue the possible relationship between D″ topography and anisotropy in this paper.

Discussion

We have used the delay times of *ScS* and S_{diff} on *SV* components of motion in relation to *SH* components to infer a long-wavelength pattern of D″ transverse isotropy beneath the northern Pacific and Alaska. This study has utilized waveforms from a data set of digitized long-period WWSSN analog records, supplemented by broadband data from recent events. In an attempt to document the first-order lateral variations in D″ properties responsible for the observed shear wave splitting, our analysis has focused on the travel time information. Below we briefly present data from two other regions, followed by further discussion of uncertainties in our approach due to the various assumptions made, and finally, we discuss possible directions for future efforts.

Figure 15a shows the wave path geometry for two other lower mantle regions: beneath the central Pacific and the Caribbean. Associated broadband displacement *SV* and *SH* observations for these wave paths are presented in Figures 15b and 15c. The data that sample the central Pacific (Figure 15b) are all along one azimuth and show no sign of S_{diff}^{sv}-S_{diff}^{sh} splitting at 95°, a very small split at 102° (0.9 s), and a 3.3 s split at 116.3°. The 3.3 s split of record 3 (Figure 15b) is comparable to that of *Vinnik et al.* [1995] for the same wave path geometry. Figure 15c shows records from a deep South American earthquake recorded by Canadian broadband stations. These records show a variety of splits: going from west to east the data display 3.1 s (record 1), 0.0 s (record 3), and 5.0 s (record 2) splitting of S_{diff}^{sv} in relation to S_{diff}^{sh} (these records were also analyzed by *Kendall and Silver* [1996]). This pattern suggests strong variations in anisotropy beneath the Caribbean, since the S_{diff} wave paths in the D″ layer for these records are only separated laterally by several hundred kilometers. This region is also noted for strong lateral variations superimposed on a background of higher than average shear velocity structure [e.g., *Bokelmann and Silver*, 1993; *Grand*, 1994] and variable D″ layer thickness [e.g., *Kendall and Nangini*, 1996].

The lower mantle region beneath the central Pacific has long been characterized as having low velocities compared to one-dimensional reference structures, from both forward modeling and tomographic inversions [e.g., *Garnero and Helmberger*, 1993]. Thus if D″ anisotropy is somehow linked to higher than average velocities, as suggested for the Caribbean and northern Pacific/Alaska regions, then the presence of D″ anisotropy beneath the central Pacific would be contrary to this trend. One possible explanation that reconciles the data of Figure 15b and the possible connection between D″ anisotropy and high velocity is as follows. The strong D″ anisotropy beneath the Caribbean and Central America (Figure 15; see also *Kendall and Silver* [1996]) may extend further north to beneath the United States, which is characterized by high lower mantle velocities [*Grand*, 1994]. A strong zone of anisotropy beneath North America (possibly extending to the west, in a manner similar to that of the high D″ velocities) could then cause S_{diff} splitting from southwest Pacific events recorded in the easternmost United States (as for record 3 in Figure 15b). This scenario would cause splitting for the largest distances having S_{diff} paths that sample beneath the western and central United States, but would result in little or no splitting for stations in the western or central United States; the central or western U.S. stations would have S_{diff} paths that miss the anisotropic zone, ascending from D″ to the west of the strong anisotropy. Thus D″ anisotropy colocated with the strong reductions in lower mantle shear velocity beneath the central Pacific may not be necessary to explain S_{diff} splits associated with southwest Pacific events recorded in the eastern United States (such as the event in Figure 15b and also those discussed by *Maupin* [1994] and *Vinnik et al.* [1995]).

A recent study by *Matzel et al.* [1996] also analyzed S_{diff} data for lower mantle structure beneath Alaska. Their conclusions are very similar to ours, namely, that strong evidence for widespread D″ anisotropy exists for this region. Our study differs, however, in some of the model details. For instance, *Matzel et al.* [1996] chose to model the S_{diff} splits with a V_{SH} structure similar to that of SYLO, but they used a V_{SV} profile with no discontinuity. This can certainly match some waveforms, but not all in our study region. We argue for the presence of a discontinuity in V_{SV} due to systematic waveform distortions in S_{diff}^{sv} (see Figure 14 and also *Lay and Young* [1991]). Such wave shapes cannot be reproduced with a structure lacking an increase in velocity at the top of D″, unless some other form of very complex structure is present. Also, our study includes ScS^{sv}-ScS^{sh} information, which proves to be the strongest evidence for splitting, since the waveform shifts are so large in relation to the path lengths in D″. By analyzing nearly 200 splitting measurements from both *ScS* and S_{diff} we are able to document the lateral variation in anisotropy in the north Pacific study area. The transverse isotropy synthetic seismograms computed by *Matzel et al.* [1996] do agree well with isotropic models for the V_{SV} and V_{SH} structures they prefer, a finding that reinforces the validity of our simplified isotropic modeling.

In using long-period data with little ray crossing we can only explore the longer wavelength D″ patterns (e.g., Figure 8c). However, this region contains significant variability at shorter wavelengths in travel times of lower mantle shear waves [*Lay and Young*, 1996; *Lay et al.*, 1997], S_{diff}^{sv} waveform shape [*Lay and Young*, 1991], and intermittence of *ScS* and S_{diff} splitting [*Lay and Helmberger*, 1983b; *Lay and Young*, 1991]. Thus it is important to keep in mind that the long-wavelength pattern we present here (Figure 8c) is an average of properties containing significant variability at much smaller scales.

We have presented evidence for a transversely isotropic D″ layer with a vertical symmetry axis. Any explanation of the cause of this anisotropy will be closely linked to the cause of the increase in seismic velocity that defines the top of the D″ layer. Some possibilities put forth for the cause of the D″ discontinuity are (1) a phase change in the lower mantle perovskite assemblage [e.g., *Nataf and Houard*, 1993], (2) scattering due to lower mantle heterogeneity [e.g., *Haddon and Buchbinder*, 1986, 1987; *Lay and Young*, 1996], and (3) a reservoir of subducted slab material [*Christensen*, 1989]. Case 1 implies a global D″ fast layer, which may be difficult to reconcile with the intense small-scale variability reported in the D″ discontinuity [e.g., *Krüger et al.*, 1993], unless such a phase change is strongly sensitive to lateral changes in temperature and/or composition. Obviously, cases 2 and 3 need not be independent, so we briefly consider case 3. If subducted material descends to the base of the mantle, where it piles up to form the D″ layer, then the intrinsic anisotropy of the subducted material may be geometrically oriented because of D″ flow. Anisotropy might depend on flow patterns and directions, thus implying azimuthal anisotropy. Azimuthal anisotropy in the lower mantle would be detected by *SKS* and has not yet been observed [see *Meade et al.*, 1995]. Alternatively, if material can accrue at the base of the mantle in a sequence of thin horizontal layers, an apparent anisotropy can result [*Backus*, 1962]. *Kendall and Silver* [1996] propose that subducted crustal material may be swept into such layers, and if that material has a much lower melting temperature than other slab components or ambient deep mantle materials, it may melt to give a strong enough velocity variation to impart a net anisotropy. Since the evidence for melting of the crustal component is at best marginal, such a model must be viewed as highly speculative. Any physical mechanism explaining the transverse isotropy will certainly have implications on lowermost mantle rheology [*Karato*, 1989; *Karato and Li*, 1992].

Preliminary particle motion analyses of our broadband data (e.g., the data of Figure 6) reveal elliptical motions. Future work will involve analyzing such motions for a larger broadband data set, including predictions from transverse isotropy synthetic seismograms. Since our method of seismogram construction only approximates transverse isotropy, we do not attempt to model the elliptical particle motions in the present effort.

Conclusions

Shear wave splitting observations for *ScS* and S_{diff} have been used to image D″ anisotropy for the lower mantle region beneath the northern Pacific and Alaska. We model the split waveforms with transverse isotropy, with $V_{SH} > V_{SV}$ in the D″ layer. A long-wavelength trend is apparent: the anisotropy is strongest in the eastern portion of our study area (≅1.5%) and smoothly tapers to zero toward the west. Waveform considerations suggest *SH* signals can be explained by a V_{SH} structure containing a 2-3% increase at the top of D″, 200-300 km above the CMB (as shown in previous studies). *SV* waveforms can be explained by a V_{SV} structure having reductions in the magnitude of the velocity increase of the V_{SH} discontinuity by up to 75%, as well as a D″ region with variations in the layer thickness. Two other regions show evidence for shear wave anisotropy, with faster velocity regions appearing to tend toward stronger anisotropy.

Acknowledgments. We thank Mike Kendall, Valerie Maupin, and Michael Wysession for thoughtful reviews, Michael Bostock for providing broadband data of the Canadian Digital Seismographic Network, Steve Grand for useful discussions and an early preprint, Mike Kendall for an early preprint, and the authors of GMT software with which all figures were constructed [*Wessel and Smith*, 1991]. Contribution #306 of the W. M. Keck Seismological Laboratory and Institute of Tectonics. This research was partially supported by NSF grant EAR9305894. E.J.G. was supported by an NSF Postdoctoral Fellowship and partially by NSF grant EAR-9628127.

References

Backus, G.E., Long-wave elastic anisotropy produced by horizontal layering, *J. Geophys. Res.*, *67*, 4427-4440, 1962.

Barruol, G., P.G. Silver, and A. Vauchez, Seismic anisotropy in the eastern United States: Deep structure of a complex continental plate, *J. Geophys. Res.*, in press, 1997.

Bataille, K., and S.M. Flatte, Inhomogeneities near the core-mantle boundary inferred from short-period scattered *PKP* waves recorded at the global digital seismograph network, *J. Geophys. Res*, *93*, 15,057-15,064, 1988.

Bokelmann, G.H.R., and P.G. Silver, The Caribbean anomaly: Short-wavelength lateral heterogeneity in the lower mantle, *Geophys. Res. Lett.*, *20*, 1131-1134, 1993.

Bullen, K.E., Compressibility-pressure hypothesis and the Earth's interior, *Mon. Not. R. Astron. Soc.*, *5*, 355-368, 1949.

Chowdhury D.K., and C.W. Frasier, Observations of *PcP* and *P* phases at Lasa at distances from 26° to 40°, *J. Geophys. Res*, *78*, 6021-6027, 1973.

Christensen, U.R., Models of mantle convection: One or several layers, *Philos. Trans. R. Soc. London, Ser. A*, *328*, 417-424, 1989.

Cormier, V.F., Synthesis of body waves in transversely isotropic Earth models, *Bull. Seismol. Soc. Am.*, *76*, 231-240, 1986.

Doornbos, D.J., Seismic wave scattering near caustics: Observations of PKKP precursors, *Nature*, *247*, 352, 1974.

Doornbos, D.J., S. Spiliopoulos, and F.D. Stacey, Seismological properties of D" and the structure of a thermal boundary layer, *Phys. Earth Planet. Inter.*, *41*, 225-239, 1986.

Dziewonski, A.M., Mapping the lower mantle: Determination of lateral heterogeneity in *P* velocity up to degree and order 6, *J. Geophys. Res.*, *89*, 5929-5952, 1984.

Dziewonski, A.M., and D.L. Anderson, Preliminary reference Earth model (PREM), *Phys. Earth Planet. Inter.*, *25*, 297-356, 1981.

Dziewonski, A.M., and J.H. Woodhouse, Global images of the Earth's interior, *Science*, *236*, 37-48, 1987.

Fouch, M.J., and K.M. Fischer, Mantle anisotropy beneath northwest Pacific subduction zones, *J. Geophys. Res.*, *101*, 15,987-16,002, 1996.

Garnero E. J., and D. V. Helmberger, Travel times of *S* and *SKS*: Implications for 3-D lower mantle structure, *J. Geophys. Res.*, *98*, 8225-8241, 1993.

Garnero, E.J., and D.V. Helmberger, A very slow basal layer underlying large-scale low-velocity anomalies in the lower mantle beneath the Pacific: Evidence from core phases, *Phys. Earth Planet. Inter.*, *91*, 161-176, 1995.

Garnero, E.J., and D.V. Helmberger, Seismic detection of a thin laterally varying boundary layer at the base of the mantle beneath the central-Pacific, *Geophys. Res. Lett.*, *23*, 977-980, 1996.

Grand, S. P., Mantle shear structure beneath the Americas and surrounding oceans, *J. Geophys. Res.*, *99*, 11,591-11,621, 1994.

Haddon, R. A. W., and G. G. R. Buchbinder, Wave propagation effects and the Earth's structure in the lower mantle, *Geophys. Res. Lett.*, *13*, 1489-1492, 1986.

Haddon, R. A. W., and G. G. R. Buchbinder, *S* wave scattering by 3-D heterogeneities at the base of the mantle, *Geophys. Res. Lett.*, *14*, 891-894, 1987.

Haddon, R. A. W., and J. R. Cleary, Evidence for scattering of seismic PKP waves near the mantle-core boundary, *Phys. Earth Planet. Inter.*, *8*, 211-234, 1974.

Inoue H., Y. Fukao, K. Tanabe, and Y. Ogata, Whole mantle *P* wave travel time tomography, *Phys. Earth Planet. Inter.*, *59*, 294-328, 1990.

Karato, S., Plasticity-crystal structure systematics in dense oxides and its implications for the creep strength of the Earth's deep interior: A preliminary result, *Phys. Earth Planet. Inter.* *55*, 234-240, 1989.

Karato, S., and P. Li, Diffusion creep in perovskite: Implications for the rheology of the lower mantle, *Science*, *255*, 1238-1240, 1992.

Kendall J.-M., and C. Nangini, Lateral variations in D″ below the Caribbean, *Geophys. Res. Lett.*, *23*, 399-402, 1996.

Kendall, J.-M., and P. M. Shearer, 1994. Lateral variations in D" thickness from long-period shear-wave data, *J. Geophys. Res.*, *99*, 11,575-11,590, 1994.

Kendall J.-M., and P. G. Silver, Constraints from seismic aniso-

tropy on the nature of the lowermost mantle, *Nature, 381*, 409-412, 1996.
Kind, R., and G. Müller, Computations of *SV* waves in realistic Earth models, *J. Geophys., 41*, 149-172, 1975.
Krüger, F., M. Weber, F. Scherbaum, and J. Schlittenhardt, Double beam analysis of anomalies in the core-mantle boundary region, *Geophys. Res. Lett., 20*, 1475-1478, 1993.
Krüger, F., M. Weber, F. Scherbaum, and J. Schlittenhardt, Evidence for normal and inhomogeneous lowermost mantle and core-mantle boundary structure under the Arctic and northern Canada, *Geophys. J. Int., 122*, 637-657, 1995.
Lavely, E. M., D. W. Forsyth, and P. Friedemann, Scales of heterogeneity near the core-mantle boundary, *Geophys. Res. Lett., 13*, 1505-1508, 1986.
Lay, T., Localized velocity anomalies in the lower mantle, *Geophys. J. R. Astron. Soc., 72*, 483-516, 1983.
Lay, T., Seismology of the lower mantle and core-mantle boundary, *U.S. Nat. Rep., Int. Union Geod. Geophys. 1991-1994, Rev. Geophys., 33*, 325-328, 1995.
Lay, T., and D. V. Helmberger, A lower mantle *S* wave triplication and the shear velocity structure of D″, *Geophys J. Int., 75*, 799-838, 1983a.
Lay, T., and D. V. Helmberger, The shear-wave gradient at the base of the mantle, *J. Geophys. Res., 88*, 8160-8170, 1983b.
Lay, T., and C. J. Young, The effect of *SKS* scattering on models of the shear velocity structure of the D" region, *J. Geophys., 59*, 11-15, 1986.
Lay, T., and C. J. Young, Analysis of *SV* waves in the core's penumbra, *Geophys. Res. Lett., 18*, 1373-1376, 1991.
Lay, T., and C. J. Young, Imaging scattering structures in the lower mantle by migration of long-period *S* waves, *J. Geophys. Res., 101*, 20,023-20,040, 1996.
Lay, T., E.J. Garnero, C.J. Young, and J.B. Gaherty, Scale-lengths of heterogeneity at the base of the mantle from *S* wave differential travel times, *J. Geophys. Res.*, in press, 1997.
Liu, X.-F., and A.M. Dziewonski, Lowermost mantle shear wave velocity structure (abstract), *Eos Trans. AGU., 75*(44), Fall Meet. Suppl., 663, 1994.
Loper, D.E., and T. Lay, The core-mantle boundary region, *J. Geophys. Res., 100*, 6397-6420, 1995.
Masters, G., and H. Bolton, Large-scale shear velocity structure of the mantle (abstract), *Eos Trans. AGU., 72*(44), Fall Meet. Suppl., 316, 1991.
Masters, G., H. Bolton, and P. Shearer, Large-scale 3-dimensional structure of the mantle (abstract), *Eos Trans. AGU., 73*, 201, 1992.
Matzel, E., M. K. Sen, and S. P. Grand, Evidence for anisotropy in the deep mantle beneath Alaska, *Geophys. Res. Lett., 23*, 2417-2420, 1996.
Maupin, V., On the possibility of anisotropy in the D″ layer as inferred from the polarization of diffracted *S* waves, *Phys. Earth Planet. Inter., 87*, 1-32, 1994.
Meade, C., P. G. Silver, and S. Kaneshima, Laboratory and seismological observations of lower mantle isotropy, *Geophys. Res. Lett., 22*, 1293-1296, 1995.
Menke, W., Effect of heterogeneities in D″ on the decay rate of P_{diff}, *J. Geophys. Res., 91*, 1927-1933, 1986a.
Menke, W., Few 2-50 km corrugations on the core-mantle boundary, *Geophys. Res. Lett., 13*, 1501-1504, 1986b.
Mitchell, B. J., and D. V. Helmberger, Shear velocity at base of mantle from observations of *S* and *ScS*, *J. Geophys. Res., 78*, 6009-6020, 1973.
Mori, J., and D.V. Helmberger, Localized boundary layer below the mid-Pacific velocity anomaly identified from a *PcP* precursor, *J. Geophys. Res., 100* 20,359-20,365, 1995.
Müller, G., The reflectivity method: A tutorial, *J. Geophys., 58*, 153-174, 1985.
Müller, G., A. M. Mula, and S. Gregersen, Amplitudes of long-period *PcP* and the core-mantle boundary, *Phys. Earth Planet. Inter., 14*, 30-40, 1977.
Nataf, H.-C., and S. Houard, Seismic discontinuity at the top of D": A world-wide feature?, *Geophys. Res. Lett., 20*, 2371-2374, 1993.
Revenaugh, J., and T. H. Jordan, Mantle layering from *ScS* reverberations, 4, The lower mantle and the core-mantle boundary, *J. Geophys. Res., 96*, 19,811-19,824, 1991.
Rogers, A., Tomographic imaging of internal Earth structure: The core-mantle boundary and the trade-off between volumetric and topographic structure, Ph.D. thesis, Univ. of Colo., Boulder, 1993.
Russo, R., and P.G. Silver, Trench-parallel flow beneath the Nazca plate from seismic anisotropy, *Science, 263*, 1105-1111, 1994.
Schlittenhardt, J., Investigation of the velocity- and Q-structure of the lowermost mantle using *PcP/P* amplitude rations from arrays at distances of 70°–84°, *J. Geophys., 60*, 1-18, 1986.
Silver, P. G., Seismic anisotropy beneath the continents: Probing the depths of geology, *Annu. Rev. Earth Planet. Sci., 24*, 385-432, 1996.
Silver, P., and W. W. Chan, Implications for continental structure and evolution from seismic anisotropy, *Nature, 335*, 34-39, 1988.
Su, W.-J., and A.M. Dziewonski, Predominance of long-wavelength heterogeneity in the mantle, *Nature, 352*, 121-126, 1991.
Su, W.-J., and A.M. Dziewonski, On the scale of mantle heterogeneity, *Phys. Earth Planet. Inter., 74*, 29-54, 1992.
Su, W.-J., R.L. Woodward, and A.M. Dziewonski, Degree 12 model of shear velocity heterogeneity in the mantle, *J. Geophys. Res., 99*, 6945-6980, 1994.
Tanimoto, T., Long-wavelength *S* wave velocity structure throughout the mantle, *Geophys. J. Inter., 100,* 327-336, 1990.
Vidale, J. E., and T. Lay, Phase boundaries and mantle convection, *Science, 261,* 1401, 1993.
Vinnik, L.V., V. Farra, and B. Romanowicz, Observational evidence for diffracted *SV* in the shadow of the Earth's core, *Geophys. Res. Lett., 16*, 519-522, 1989.
Vinnik, L.V., B. Romanowicz, Y. Le Stunff, and L. Makeyeva, Seismic anisotropy of the D" layer, *Geophys. Res. Lett., 22*, 1657-1660, 1995.
Weber, M., P and *S* wave reflections from anomalies in the lowermost mantle, *Geophys. J. Int., 115,* 183-210, 1993.
Weber, M., and M. Kornig, Lower mantle inhomogeneities inferred from PcP precursors, *Geophys. Res. Lett., 17*, 1993-1996, 1990.
Weber, M., and M. Kornig, A search for anomalies in the lowermost mantle using seismic bulletins, *Phys. Earth Planet. Inter., 73*, 1-28, 1992.
Wessel, P., and W.H.F. Smith, Free software helps map and display data, *Eos Trans. AGU, 72*, 441, 445-446, 1991.
Woodward, R.L., and G. Masters, Lower-mantle structure from *ScS-S* differential travel times, *Nature, 352*, 1991.
Wysession, M. E., Continents on the core, *Nature, 381*, 373-374, 1996.
Wysession, M. E., and E. A. Okal, Evidence for lateral heterogeneity at the core-mantle boundary from the slowness of diffracted *S* profiles, in *Structure and Dynamics of Earth's Deep Interior, Geophys. Monogr. Ser.*, vol. 46., edited by D. E. Smylie and R. Hide, pp. 55-63, AGU, Washington, D. C., 1988.
Wysession, M. E., and E. A. Okal, Regional analysis of D″ velocities from the ray parameters of diffracted *P* profiles, *Geophys. Res. Lett., 16,* 1417-1420, 1989.
Wysession, M. E., E. A. Okal, and C. R. Bina, The structure of the core-mantle boundary from diffracted waves, *J. Geophys. Res., 97*, 8749-8764, 1992.
Wysession, M. E., L. Bartko, and J. Wilson, Mapping the lowermost mantle using core-reflected shear waves, *J. Geophys. Res., 99*, 13,667-13,684, 1994.
Young, C. J., and T. Lay, Multiple phase analysis of the shear velocity structure in the D" region beneath Alaska, *J. Geophys. Res., 95,* 17,385-17,402, 1990.

E.J. Garnero and T. Lay, Institute of Tectonics, Earth Sciences Board, University of California, Santa Cruz, CA, 95064. (e-mail: eddie@rupture.ucsc.edu; thorne@plume.ucsc.edu)

(Received June 21, 1996; revised December 2, 1996; accepted December 9, 1996.)